Dimers to Doughnuts: Redox-Sensitive Oligomerization of 2-Cysteine Peroxiredoxins[†,‡]

Zachary A. Wood,[§] Leslie B. Poole,[||] Roy R. Hantgan,[||] and P. Andrew Karplus*[,§]

Department of Biochemistry and Biophysics, Oregon State University, Corvallis, Oregon 97331,
and Department of Biochemistry, Wake Forest University School of Medicine, Winston-Salem, North Carolina 27157

ABSTRACT: 2-Cys peroxiredoxins (Prxs) are a large and diverse family of peroxidases which, in addition to their antioxidant functions, regulate cell signaling pathways, apoptosis, and differentiation. These enzymes are obligate homodimers (α_2), utilizing a unique intermolecular redox-active disulfide center for the reduction of peroxides, and are known to form two oligomeric states: individual α_2 dimers or doughnut-shaped $(\alpha_2)_5$ decamers. Here we characterize both the oligomerization properties and crystal structure of a bacterial 2-Cys Prx, *Salmonella typhimurium* AhpC. Analytical ultracentrifugation and dynamic light scattering show that AhpC's oligomeric state is redox linked, with oxidization favoring the dimeric state. The 2.5 Å resolution crystal structure ($R = 18.5\%$, $R_{\text{free}} = 23.9\%$) of oxidized, decameric AhpC reveals a metastable oligomerization intermediate, allowing us to identify a loop that adopts distinct conformations associated with decameric and dimeric states, with disulfide bond formation favoring the latter. This molecular switch contains the peroxidatic cysteine and acts to buttress the oligomerization interface in the reduced, decameric enzyme. A structurally detailed catalytic cycle incorporating these ideas and linking activity to oligomeric state is presented. Finally, on the basis of sequence comparisons, we suggest that the enzymatic and signaling activities of all 2-Cys Prxs are regulated by a redox-sensitive dimer to decamer transition.

The alkyl hydroperoxide (Ahp) reductase system is part of an essential peroxide-inducible response to oxidative stress found in many bacteria (*1−6*). This system consists of two soluble components, AhpF[1] and AhpC, which together catalyze the NADH-dependent reduction of organic hydroperoxides (or hydrogen peroxide) to their corresponding alcohols and water (*7, 8*). AhpF, an FAD-dependent NADH: protein disulfide reductase whose structure (*9, 10*) and mechanism (*11−15*) have been well studied, acts to reduce AhpC. AhpC is the peroxidase of the system, and the enzyme from *Salmonella typhimurium* is the focus of this paper.

* To whom correspondence should be addressed at the Department of Biochemistry and Biophysics, Oregon State University, Corvallis, OR 97333. E-mail: karplusp@ucs.orst.edu.
[§] Department of Biochemistry and Biophysics, Oregon State University.
[||] Department of Biochemistry, Wake Forest University School of Medicine.

[1] Abbreviations: AhpC, alkyl hydroperoxide reductase peroxidase component, member of the peroxiredoxin family; Prx, peroxiredoxin; AhpF, alkyl hydroperoxide reductase flavoprotein or NADH:peroxiredoxin oxidoreductase; MAD, multiwavelength anomalous dispersion; Se-Met, selenomethionine; FPLC, fast protein liquid chromatography.

Scheme 1
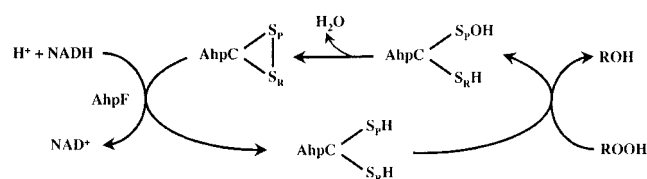
As shown in Scheme 1, AhpC has two redox-active cysteines: one, the peroxidatic cysteine (S_P), attacks the peroxide substrate (ROOH) and becomes oxidized to a sulfenic acid, and then the resolving cysteine (S_R) attacks the cysteine-sulfenic acid to release water and form a disulfide bond (*16, 17*). The disulfide form of AhpC is reduced by AhpF to complete the catalytic cycle.

AhpC is a member of the recently described 2-Cys peroxiredoxin (Prx) family, with homologues found in all kingdoms (*18−21*). Like all 2-Cys Prxs, *S. typhimurium* AhpC is an obligate homodimer (α_2) with the peroxidatic cysteine from one monomer and the resolving cysteine from the other forming an intersubunit redox-active disulfide (*16, 17*). In addition to their antioxidant functions, eukaryotic 2-Cys Prxs have been shown to modulate the apoptotic pathways that are activated by p53 (*22, 23*), tumor necrosis factor (TNF) (*24−26*), and the anticancer drug cisplatin (*27*). High levels of expression of 2-Cys Prxs are strongly correlated with resistance to cisplatin (*27*) and protection of tumors during radiation therapy (*28*).

Recently, it has been reported that 2-Cys Prxs will oligomerize in solution to form decamers (*29−32*). The crystal structures of three different of 2-Cys Prxs have

revealed two distinct oligomeric forms: the structure of the disulfide form of heme binding protein 23 (HBP23) at 2.7 Å resolution is an α_2 dimer (*33*), and both the reduced tryparedoxin peroxidase (TryP) from *Crithidia fasiculata* at 3.2 Å resolution (*34*) and the thioredoxin peroxidase B (TPx-B) from human erythrocytes at 1.7 Å resolution (*29*) are ($\alpha_2)_5$ decamers. Although the TPx-B structure has its peroxidatic cysteine oxidized to an inactive sulfinic acid, the authors propose that it faithfully represents the reduced form of the enzyme (*29*).

The factors that govern the oligomeric assembly of 2-Cys Prxs are not well understood. One report suggests that high ionic strength drives the oligomerization and activity of a bacterial 2-Cys Prx (*30*), whereas another suggests the opposite, that high ionic strength leads to dissociation of the decamer (*32*). Still other reports have indicated that oligomerization is dependent on pH, with lower pHs favoring oligomerization (*31*), or on redox state, with reduction of the enzyme resulting in oligomerization (*35*). In the case of TPx-B, the authors combine these ideas and propose that in vivo both a change in ionic strength and a small drop in pH during times of oxidative stress act to drive oligomerization to the ($\alpha_2)_5$ decamer and that formation of the active site disulfide bond favors the dimeric structure (*29*).

Two separate structural comparisons between decameric and dimeric forms of 2-Cys Prxs have revealed specific details of the oligomeric assembly and have led to proposed mechanisms for the decamer to dimer transition (*29, 34*). Although both reports identify the same key players, the proposed order of events and driving forces is different. More specifically, both authors identify that a local unfolding in the active site is correlated with disulfide bond formation and structural rearrangements in the oligomerization interface. Schroder et al. (*29*) propose that it is the local unfolding coincident with the shift of a surface loop that forces the structural rearrangements in the interface, and this promotes decamer dissociation and disulfide bond formation. On the other hand, Alphey et al. (*34*) propose that the nucleophilic attack of the resolving cysteine on the peroxidatic cysteine-sulfenic acid promotes the structural rearrangements in the interface and drives apart the decamer. In their comparisons, both authors were limited in that they had only two forms of the enzyme available for analysis, the reduced decamer and the disulfide containing dimer, making it impossible to distinguish events that occur immediately prior to dissociation from those stuctural rearrangements that occur afterward.

Here, we present studies that resolve questions regarding the control and mechanism of 2-Cys peroxiredoxin oligomerization. First, we demonstrate that the oligomerization of *S. typhimurium* AhpC is primarily redox sensitive, with the reduced enzyme strongly favoring the ($\alpha_2)_5$ decamer and with the oxidized enzyme forming a mixture of predominantly lower order oligomeric assemblies. Second, we present a 2.5 Å resolution crystal structure of the disulfide form of decameric AhpC. This represents an important, metastable intermediate between reduced decamers and oxidized dimers. This structure, in comparisons with the other available 2-Cys Prx structures, allows identification of the molecular switch responsible for the disassociation of the decamer. Finally, we incorporate these ideas in a structurally detailed catalytic cycle and present a testable hypothesis that oligomeric state is linked to enzyme activity and signaling.

EXPERIMENTAL PROCEDURES

Purification of AhpC and Se-Met AhpC. AhpC was expressed and purified essentially as described previously (*8*). For selenomethionine (Se-Met) incorporation, the same plasmid (pAC1) was transformed into the methionine auxotroph B834(DE3) (Novagen, Inc., Madison, WI). Expression of Se-Met AhpC followed methods used previously by Ramakrishnan et al. (*36*). The medium consisted of $2\times$ M9 salts supplemented with 0.4% glucose, amino acids (excluding methionine) at 40 mg/mL each, seleno-L-methionine from Sigma at 40 mg/mL, and four vitamins (riboflavin, niacinamide, pyridoxine monohydrochloride, and thiamin) at 1 mg/mL each. Chloramphenicol at 25 mg/mL was included. A 1.0 L culture in the above medium was grown overnight (about 16 h) at 37 °C to $A_{600} = 1.4$. IPTG was added and incubation continued for an additional 6 h. Purification of Se-Met AhpC as previously described (*8*) yielded 19 mg that was concentrated to 10 mg/mL in 25 mM potassium phosphate, pH 7.0, and 1 mM EDTA and stored at −20 °C.

Analytical Ultracentrifugation. Sedimentation velocity and equilibrium analyses were performed at 20 °C using an Optima XL-A analytical ultracentrifuge (Beckman Instruments, Palo Alto, CA). AhpC [with or without 1 h pretreatment with a 20-fold excess of dithiothreitol (DTT)] was concentrated and exchanged into 25 mM potassium phosphate, 1 mM EDTA, and 0.15 M NaCl, pH 7, using CM-30 Centricon ultrafiltration units (Millipore Corp.) or 10K cutoff Apollo concentrators (Orbital Biosciences, Topsfield, MA); the buffer for reduced AhpC contained freshly added 100 μM DTT. A value of 0.7370 cm^3/g was calculated for the partial specific volume of AhpC from the amino acid composition (*37*), and the buffer density, at 1.0077 g/cm^3, was measured using a DA-310 precision density meter (Mettler Toledo, Hightstown, NJ). Data were collected at 280 nm (or at 250 nm for [AhpC] > 55 μM and at 230 nm for [AhpC] < 9 μM). Only data of less than 1.4 absorbance units were used.

Sedimentation velocity experiments were carried out using double-sectored Epon charcoal cells (12 mm path length for most samples, 3 mm path length for the highest concentration). For each concentration, sedimentation and diffusion coefficient values of AhpC were calculated using the Fujita−MacCosham function based on the Lamm equation and the SVEDBERG (version 6.23) software (*38, 39*) and DCDT sofware (*40*) (www.jphilo.mailway.com).

These parameters were standardized to pure water (correcting for density and viscosity) (*37*) and extrapolated to zero concentration. The molecular weight (M_w) of AhpC was calculated from the Svedberg equation (*41*) using the $s^0_{20,w}$ values and the corrected translational diffusion coefficients ($D^0_{20,w}$). Samples prepared at each dilution were incubated for at least 90 min at 20 °C before beginning the centrifugation. Sedimentation data for 430 μL each of 2.5, 12, and 25 μM reduced AhpC were collected every 3 min at a rotor speed of 42 000 rpm and a radial step size of 0.003 cm. Oxidized AhpC was analyzed in a similar way, except that 11 concentrations from 2.5 to 483 μM were analyzed at rotor speeds from 35000 to 52000 rpm.

Sedimentation equilibrium experiments with reduced AhpC were performed essentially as described previously

(*12*). For reduced (DTT-treated) AhpC, five concentrations (6.2−107 μM) were analyzed in six-sectored cells at 5500, 6500, 8000, and 11000 rpm. For oxidized AhpC, speeds of 8000, 11000, 15000, 20000, and 26000 rpm were used, and protein concentrations were varied from 2.5 to 107 μM. Equilibration times were 14, 16, and 18 h. Global analysis of data sets was performed using the Windows version of NONLIN (*42*).

Light-Scattering Methods. Light-scattering data were acquired using a Brookhaven Instrument BI-2030AT correlator, operated together with a BI-200SM light-scattering goniometer/photon counting detector (Brookhaven Instruments, Holtsville, NY) and a Spectra Physics 127 helium−neon laser (35 mW, equipped with a vertical polarization rotator; Spectra Physics, Mountain View, CT). For determination of the molecular weight of oxidized and reduced AhpC by static light-scattering analyses, measurements were made at an angle of 90° in specially formulated microcuvettes (Hellma Cells, Inc.) maintained at 20 °C in a refractive index matching bath (containing 50% glycerol). Samples in the 25 mM potassium phosphate buffer with or without NaCl were passed through a 0.2 μm filter, and the filtrate was collected into acid-washed, dust-free microcuvettes. Sample scattering intensities were corrected for solvent scattering and were expressed relative to a benzene standard (*43*). AhpC concentrations were measured at 280 nm using an $E^{0.1\%}$ value of 1.18 (*8*). A total of 18 intensity measurements for reduced AhpC (37−57 μM) and 30 for oxidized AhpC (45−346 μM) were used for molecular weight calculations. Weight-average molecular weights were determined from the solvent-corrected relative scattering intensity using Rayleigh−Gans−Debye theory (*44*) and a protein refractive index increment (dn/dc) of 0.183 mL/g as calculated from the amino acid composition (*45*). Dynamic light scattering was also carried out with the above samples to determine the translational diffusion coefficient [$D^0_{20,w}$ (*41*)] using the method of cumulants as described previously (*46*).

Crystallization of AhpC. Using hanging drops and the sparse matrix strategy (*47*), a crystallization lead was identified that, when optimized, gave reproducible crystals for native and Se-Met AhpC at 26 °C using 1.4 M magnesium sulfate, 0.1 M MES, pH 6.5, as a reservoir, and 5 μL of a 10 mg/mL stock solution of AhpC mixed with 2 μL of the reservoir for the drop. Crystals appeared within 2 weeks, reaching sizes on the order of 1 mm in each dimension. The crystals were very fragile and difficult to manipulate. For data collection, crystals were dipped (~20 s) into a cryoprotectant solution containing 20% (w/v) glycerol in addition to the reservoir solution above and then either flash cooled in a −170 °C nitrogen stream or plunged into liquid nitrogen (*48*).

X-ray Diffraction Data Collection and Processing. The space group of the crystals is $C222_1$ with $a = 127.5$ Å, $b = 171.6$ Å, and $c = 135.8$ Å, but this was not recognized early on, and the structure solution was done using the space group $P2_1$ with unit cell $a = 106.9$ Å, $b = 135.9$ Å, $c = 107.2$ Å, and $\beta = 106.8°$. A 2.5 Å resolution native data set was collected at beamline 5.0.2 of the Advanced Light Source (ALS) from a single frozen crystal of AhpC. Using an ADSC Quantum-4 mosaic CCD-based X-ray detector (Area Detector System Corp.), 180° of data were collected (40 s per 1° frame). A three-wavelength MAD data set was collected from

a single crystal of Se-Met AhpC at beamline F2 of the Cornell High Energy Synchrotron Source (CHESS) using an ADSC Quantum-4 X-ray detector. A fluorescence scan determined the optimum wavelengths to minimize the f' (edge) and to maximize the f'' (peak) contributions. Due to time constraints, the remote was chosen 100 eV lower than the peak to avoid the need to collect Bijvoets. On the basis of the crystal orientation, the optimal strategy for a >90% complete, 3.0 Å resolution data set required 90° of data. Using the inverse beam method, complete data sets were collected in 5° wedges (40 s per 1° frame) for the edge and peak wavelengths.

All frames were corrected for background, spatial distortion, and nonuniformity. Native data (Table 1) were processed using the HKL suite of programs (*49*). The program NovelR calculated the multiplicity-weighted merging R-factor (*50*). The MAD data sets (Table 1) were processed using the CCP4 programs MOSFLM and SCALA (*51*).

Locating the Se Sites and MAD Phasing. The f' and f'' for each wavelength were estimated using the program FPRIME (*52*, *53*). Using data to 3.5 Å resolution, the program SOLVE identified and refined 16 sites, resulting in phases with a figure of merit ($\langle m \rangle$) of 0.57. Difference maps (*54*) calculated with these phases revealed positions for four additional Se atoms corresponding to a total of ten AhpC molecules in the asymmetric unit (assuming two Se-Met per chain), and phases to 3 Å resolution were then calculated ($\langle m \rangle = 0.66$). The resulting electron density maps displayed clear protein−solvent boundaries, as well as easily recognizable helices and sheets. Using the program suite PHASES (*55*), the 3 Å resolution MAD electron density map was subjected to 16 cycles of solvent flattening assuming 50% solvent. The resulting map was of high quality and allowed the identification of 10 molecules arranged as a doughnut-shaped decamer. Noncrystallographic symmetry (NCS) operators between all ten molecules were defined using X-PLOR (*56*), and then NCS density averaging and solvent flattening were carried out using PHASES.

Model Building and Refinement. Model building was carried out using the programs CHAIN (*57*) and O (*58*). The density for all ten molecules was averaged using RAVE (*59*−*61*), and the resulting map allowed the tracing of the majority of one molecule by placing Cα atoms and then using the LEGO autobuild feature of O. The NCS symmetry operators were applied to this model to construct the unique contents of the monoclinic unit cell. This initial model represented 91% of the final model. Five percent of the data were set aside for cross-validation. Initially, model refinement was carried out using X-PLOR and data to 3 Å resolution. Rigid body refinement was performed on all ten molecules, followed by simulated annealing using Cartesian molecular dynamics with NCS restraints against the crystallographic residual target. This reduced the R-factor from an initial high of 48.9% to 35.6% ($R_{\text{free}} = 39.7\%$). At this point we switched to the native data set while preserving the cross-validation test set and extended the resolution to 2.5 Å. Further cycles of simulated annealing, individual B-factor refinement, and manual rebuilding reduced the R-factor to 30.4% ($R_{\text{free}} = 33.2\%$). For the final stages of model refinement, we used the program CNS (*62*) and abandoned simulated annealing in favor of Powell minimization using the maximum likelihood target function. For individual B-factor refinement, the

Table 1: Data Collection Statistics

data set	native	peak[a]	edge[a]	remote[a]
wavelength (Å)	1.1000	0.9796	0.9798	0.9873
resolution (Å)	2.5	3.0	3.0	3.0
total observations	374091	100569	198239	197790
unique reflections	51663	53055	53131	52939
completeness	97.4 (92.2)[b]	92.3 (84.8)	91.9 (82.4)	91.8 (82.6)
I/σ	16.0 (4.5)	16.0 (5.2)	24.4 (7.9)	23.6 (7.4)
R_{meas}[c]	8.0 (51.8)	7.2 (35.5)	6.0 (25.2)	6.6 (27.5)
R_{mrgd-F}[d]	7.1 (35.5)	nd[e]	nd	nd
MAD difference ratios[f]	peak	0.051 (0.032)	0.035	0.051
	edge		0.049 (0.036)	0.049
	remote			nd

[a] Mistakenly treated as lower symmetry $P2_1$ space group (see Experimental Procedures). [b] Numbers in parentheses represent the highest resolution shell. [c] R_{meas} is the multiplicity weighted merging R-factor of Diederichs and Karplus (*50*). [d] R_{mrgd-F} is a measure of reduced data accuracy (*50*). [e] Not determined. [f] MAD difference ratios were determined using the program MADSYS (*76*). Ratios are $\text{rms}(|\Delta F|)/\text{rms}(|F|)$, where ΔF is the Bijvoet difference within a wavelength (diagonal elements) or the dispersive difference between wavelengths (off-diagonal elements). F is the average value of the structure factor for that energy. The values in parentheses are for centric reflections, which ideally should be zero and therefore represent the level of noise in the anomalous signal. For the low-energy remote, Bijvoets were merged and only dispersive differences were used in phasing (see Experimental Procedures).

Table 2: Crystallographic Refinement Statistics

resolution range (Å)	50.0−2.5
amplitude cutoff	none
no. of amino acid residues	825
no. of sulfates	3
no. of waters	273
total non-H atoms	6789
average B (Å^2)	
protein	53
solvent	44
R-factor (%)	18.5
free R-factor (%) (10% of data)	23.9[a]
stereochemical ideality	
bond length rmsd (Å)	0.014
bond angle rmsd (deg)	1.6
ϕ,ψ most favored (%)	90.0
ϕ,ψ additional allowed (%)	9.9
ϕ,ψ generously allowed (%)	0.1

[a] Posteriori calculated R_{free} (see Experimental Procedures).

crystallographic residual target was used. Waters were added both manually and using the Water-Pick utility in CNS (*62*) with the following criteria: (1) a minimum $3\rho_{rms}$ peak in $F_o − F_c$ maps and (2) a minimum distance of 2.6 Å and a maximum distance of 3.5 Å to donors or acceptors. Finally, sulfates were added on the basis of the hydrogen-bonding environment.

After refinement was complete we discovered our space group assignment error and reindexed as $C222_1$. The higher symmetry leaves only five molecules in the asymmetric unit and invalidates the original R_{free} test set. A new test set representing 10% of the data was selected, and the new model was subjected to simulated annealing using Cartesian molecular dyanmics at 4000 K to decouple the test set (*63*). The final model statistics are reported in Table 2.

The active site disulfide bonds are exposed and are relatively mobile, as evidenced by weak electron density and high B-factors. To verify that the disulfide state of the enzyme was modeled correctly, the C-termini of all molecules were removed past residue Glu163, including the resolving cysteine, Cys165. The omit model was then subjected to simulated annealing at 5000 K, followed by individual B-factor refinement. The resulting electron density maps revealed clear density for the omitted residues, including the cystine disulfide (Figure 2A).

Examination of the modeled waters reveals that five, all related by NCS symmetry, are suspicious (W1 to W5). The B-factors for these five waters are one-half the value of their corresponding ligands, with hydrogen-bonding distances of ∼3.0 Å. We suspect these waters may actually be metals or halides, but in the absence of an identification we have left them modeled as water molecules.

Structure and Sequence Analysis. Model quality was assessed using PROCHECK (*64*) and the model check routine in CNS (*62*). Secondary structure assignments were

made using DSSP (*65*). Topology diagrams were constructed with TOPS (*66*). Sequence alignments were done using PIMA (*67, 68*). HOMOLOGCORE (P. A. Karplus) was used to create structural overlays for comparisons. Structural figures were generated using MOLSCRIPT (*69*), BOB-SCRIPT (*70*), and RASTER3D (*71*).

RESULTS AND DISCUSSION

The Oligomeric State of AhpC Is Redox Sensitive. Sedimentation velocity, sedimentation equilibrium, and light scattering at varying protein concentrations were used to study the size and shape of AhpC and how it is influenced by the redox state (Table 3). As summarized in Figure 1 and Table 3, sedimentation velocity experiments were the most informative. At all concentrations studied, reduced AhpC data were well fit by a single Gaussian (Figure 1), consistent with the presence of a homogeneous 8.7 S species corresponding to a weight-averaged molecular weight (M_w) of 214 kDa. Given that the M_r of monomeric AhpC is 20.6 kDa, these results suggest an oligomeric complex of 10 subunits. This agrees well with our observations (see below) and those of others that 2-Cys peroxiredoxins form stable decameric complexes (*29−32*). On the other hand, oxidized AhpC yielded results that were concentration dependent (Figure 1). Only at the limiting concentrations evaluated did oxidized AhpC behave as a homogeneous species. At the lower limit (2.5 μM), oxidized AhpC had a value of 3.35 S and a calculated M_w of 40 kDa, corresponding to dimeric AhpC (Table 3). At the upper limit (483 μM), oxidized AhpC yielded a value of 6.67 S and a calculated M_w of 227 kDa, consistent with decameric AhpC. In experiments using intermediate concentrations (9−330 μM), a wider and more complex distribution of S values were detected, indicating a heterogeneous system, presumably involving dimers, decamers, and possibly intermediate species (Figure 1).

In addition to determining oligomeric states of a protein, sedimentation velocity experiments can be used to derive shape information. For reduced AhpC, the measured $D^0_{20,w}$ value is 1.42-fold smaller than that expected for a spherical molecule of 206 kDa and corresponds to that expected for a highly oblate ellipsoid with an axial ratio of ∼9:1, consistent with the doughnut-shaped structure we report below. A further intriguing observation is that decameric AhpC in its oxidized and reduced forms exhibits two different sedimen-
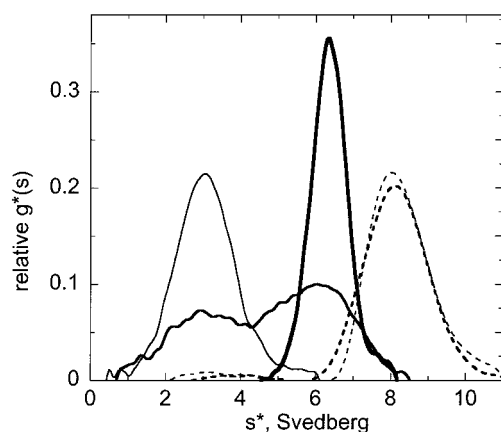
FIGURE 1: Sedimentation velocity studies of oxidized and reduced AhpC. Oxidized (solid lines) and reduced (dashed lines) AhpC samples at 2.5 μM (thin lines), 12 μM (medium thick lines), and 483 μM (thickest solid line) were centrifuged at 42000 (dashed lines and thick solid line) or 47000 rpm (thin and medium solid lines). Eight to twelve consecutive data sets at $\Delta\omega^2t$ values of 0.25 to 0.55 × 10^{11} s^{-1} were analyzed by DCDT software (*40*) to give the g^* (s) distributions shown. All plots were normalized by area to ease comparisons.

Table 3: Sedimentation and Light-Scattering Analyses of Oxidized and Reduced AhpC

	reduced AhpC	oxidized AhpC
M_w by sedimentation equilibrium (kDa)	198 ± 3[a]	42[b]
M_w from s^c and D^d (kDa)	214	40, 227[c,e]
sedimentation coeff ($s^0_{20,w}$)[c,f] (S)	8.70	3.35, 6.67[e]
translational diffusion coeff ($D^0_{20,w}$)[d,g] (F)	3.88	7.90, 2.79[e]

[a] From 17 data sets (χ^2 = 5.74 × 10^{-4} with 1521 degrees of freedom). [b] At 2.5 μM and 26 000 rpm. [c] From sedimentation velocity analyses. [d] Diffusion coefficient from dynamic light-scattering analyses. [e] Values from samples at 2.5 and 483 μM, respectively. [f] In Svedbergs, ×10^{-13} s. [g] In Ficks, ×10^{-7} cm^2s^{-1}.

tation coefficients, at 6.7 and 8.7 S, respectively (Figure 1). This suggests a significant difference between the two species. Because no such difference is apparent in the crystallographic results (see below), we suspect the distinct sedimentation properties are due to the presence of a dynamic equilibrium in oxidized AhpC among different decameric states and/or lower order oligomers.

Sedimentation equilibrium and light-scattering results were less informative but consistent with the above observations. Sedimentation equilibrium experiments with reduced AhpC exhibited no dependence on either protein concentration or speed (data not shown). Using the single ideal species model, a M_w of 198 ± 3 kDa was calculated (Table 3). Sedimentation equilibrium experiments with oxidized AhpC gave complex results, consistent with the expected heterogeneous nature of the species. In addition, as analysis time increased from 24 to 48 h, a systematic increase in molecular weight estimates was observed, suggesting an irreversible aggregation over long periods of time. At present, we do not understand this behavior and, therefore, view the results with caution. The only easily modeled sedimentation equilibrium analysis of oxidized AhpC was that at the lowest concentration and highest speed. The results yielded a limiting M_w for the associating species of 42 kDa, again consistent with dimeric AhpC (Table 1). Static light-scattering experiments were limited to protein concentrations between 44 μM and

346 μM due to signal to noise considerations at lower concentrations and nonideal behavior at higher concentrations. All light-scattering analyses using reduced AhpC gave a M_w of ca. 196 kDa, but analyses of oxidized AhpC gave M_w values that generally increased as a function of concentration and were all between the expected dimer and decamer weights, consistent with a mixture of species. To assess how ionic strength influenced AhpC oligomerization, further sedimentation and light-scattering studies were performed with both reduced and oxidized AhpC in the presence of increasing salt. Contrary to a previous report (*30*), we noticed no effect of low ionic strength (up to 0.15 M NaCl) and little effect of high ionic strength (up to 1.0 M NaCl) on the oligomeric structure of either redox form of AhpC (data not shown).

From all these data, we conclude that reduced AhpC in solution forms a rather stable decamer, and oxidized AhpC has a much weaker association constant so that it forms a concentration-dependent mixture of oligomeric species ranging from free dimers to decamers. Using data from Link et al. (*72*) and a value of 2.5 fL for the volume of *Escherichia coli*, we estimate the in vivo concentration of AhpC to be ~5 μM. On the basis of our results and in the absence of other factors, oxidized AhpC would tend to be in the dimeric state. This suggests that in vivo there is a direct linkage of redox state and oligomerization.

Crystal Structure of Oxidized AhpC. Crystals of AhpC are very fragile, and the structure was solved using MAD phasing (see Experimental Procedures). The resulting 2.5 Å resolution crystal structure reveals that the enzyme is in the oxidized, disulfide form (Figure 2A). The asymmetric unit of the crystal contains five molecules (chains A−E), with the biologically relevant decamer generated by a crystallographic 2-fold symmetry operation (chains A′−E′). The resulting complex is a doughnut-shaped pentamer of homodimers or an (α_2)$_5$ decamer displaying point group symmetry 52 (Figure 2B). The decamer has an outer diameter of 115 Å, inner diameter of 60 Å, and thickness of 45 Å and looks very similar to the structures of TryP and TPx-B (*29, 34*). The C-terminus is disordered past residue Pro166 in molecules A and D, past Cys165 in molecules B and E, and past Glu163 in molecule C.

Our observation of an oxidized, decameric form of AhpC is suprising, given our results (above) demonstrating that the (α_2)$_5$ oligomer is destabilized upon oxidation. However, given the concentration dependence on the oligomeric state of oxidized AhpC (Figure 1), the high protein concentration during crystallization (ca. 900 μM) explains why decamers were formed. This suggests that we have crystallized a metastable intermediate: a weakly associated decamer.

The Basic Oligomeric Building Block: The α_2 Dimer. Each AhpC monomer consists of a central seven-stranded β-sheet sandwiched between four α-helices on one face and a β-hairpin and two α-helices on the other. The overall topology of AhpC is essentially the same as that described for other 2-Cys Prxs (*29, 33, 34*), containing a thioredoxin fold with few additional secondary structure elements. Overlaying the AhpC monomer with the structures of TryP, TPx-B, and the heme binding protein 23 (HBP23) results in rms deviations for 161 corresponding Cα atoms of 1.4, 1.5, and 1.6 Å, respectively, with only minor differences in secondary structure (Figure 3).

A.

B.

C.
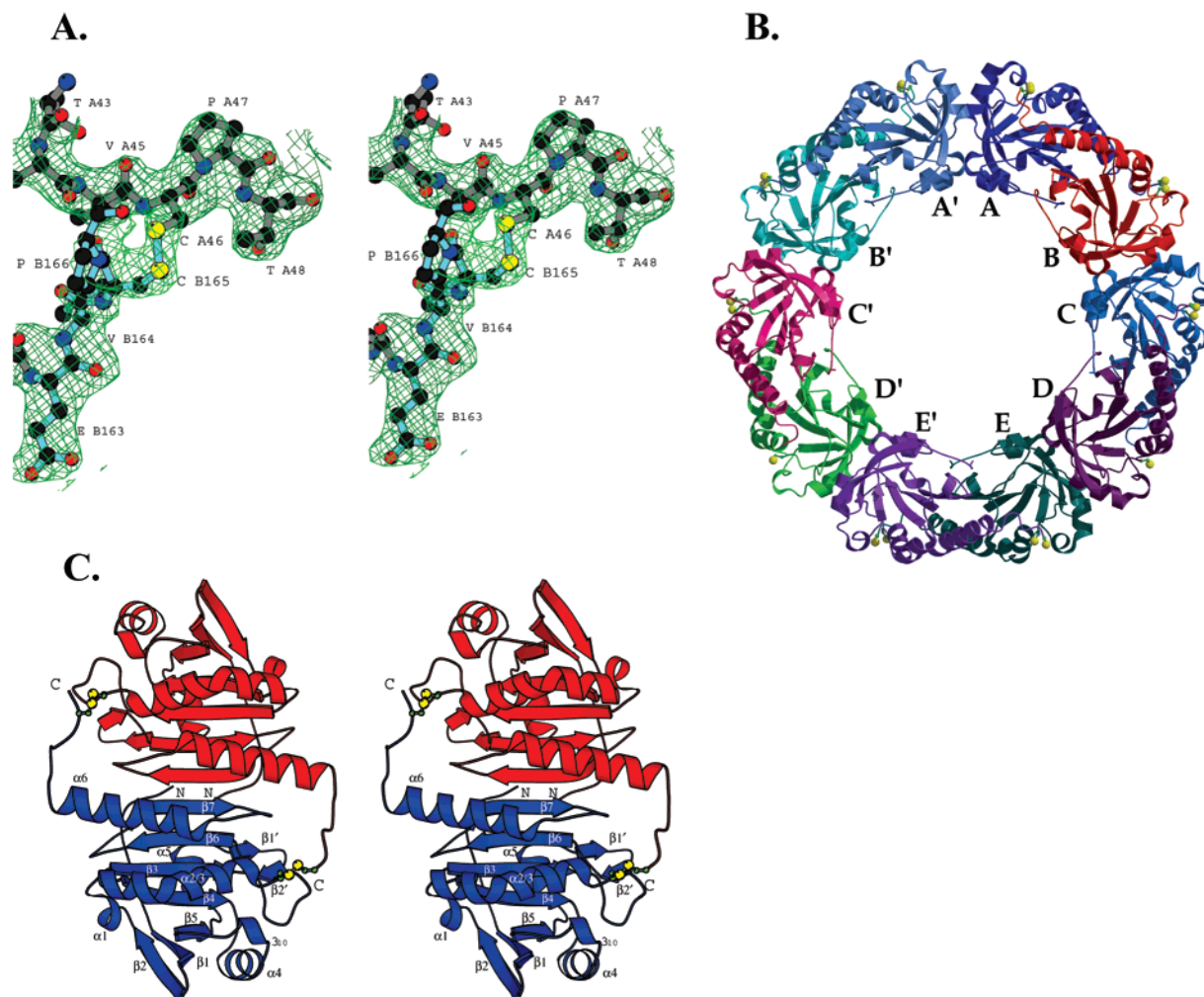
FIGURE 2: Structure of oxidized AhpC. (A) Electron density for the redox-active disulfide. The $2F_o - F_c$ electron density map shown was calculated after removing the residues C-terminal to Gly162, including the resolving cysteine, for all five molecules and subjecting the resulting omit model to simulated annealing. The density is contoured at $1.4\rho_{rms}$. The model (gray for residues not omitted, cyan for omitted residues) is the final model of the A–B dimer, with residues from chain A (residues 44–48) and chain B (residues 163–165). This is the best defined disulfide in the structure. (B) $(\alpha_2)_5$ decamer of AhpC. Each chain is depicted in a different color, and the unique molecules are labeled A, B, C, D, and E, with primes denoting their crystallographic symmetry mates. Dimers are A–B, C–D, and E–E'. The crystallographic 2-fold axis bisects the homodimer (E–E') and the interface between the two adjacent dimers (A–B and A'–B'). Redox-active disulfides are depicted as ball-and-stick models, with sulfurs in yellow. (C) Stereoview of the AhpC dimer, with monomers in different colors and looking down the dimer axis. The intermolecular redox-active disulfides are depicted as above. The C-terminal arm containing the resolving cysteine reaches across the interface and is rather flexible.

Dimerization results in an extended β-sheet containing 14 strands (7 from each monomer) with the interface formed between the antiparallel strands β7 and β7' (Figure 2C). The dimer interface buries ~2100 Å^2 of surface area and involves 56 residues (~1050 Å^2 and 28 residues from each monomer). The α$_2$ dimer forms a flattened ellipsoid with dimensions 60 Å × 45 Å × 30 Å, similar to what has been described previously for 2-Cys peroxiredoxins (*29, 34*) (Figure 2C). Each dimer contains two identical active sites 41 Å apart with the C-terminus (residues 159'–166') reaching across the dimer interface to form the intermolecular redox-active disulfide (Cys46 with Cys165'). Since we have solved the structure of the disulfide form of AhpC, we have no new information about the geometry of the peroxidatic active site to add to what has already been covered on the basis of the reduced structures (*29, 34*). We will instead focus on the valuable insights into the oligomeric assembly that can be gained from examining this unique, intermediate structure.

Oligomerization Interface in Oxidized AhpC. The interface between α$_2$ dimers as they oligomerize to form decamers buries ca. 650 Å^2 of surface area per monomer in three hydrophobic patches containing 20 residues (Figure 4A). The majority of these residues are localized in four segments of the protein: region I (residues 40–44), region II (residues 73–84), region III (residues 99–100), and region IV (residues 112–116) (Figure 3). Region I forms a surface which is complementary to region II, and these two patches, with the inclusion of Phe20, overlap to form the largest buried patch (ca. 450 Å^2) in the interface (Figure 4B). The remaining two contacts in the interface are formed by less extensive hydrophobic interactions (ca. 100 Å^2 each) between region III of each dimer and its complementary region IV. Although region IV contains many charged residues (three of five), it is only the allylic portions that contribute to the hydrophobic interface, with the charged headgroups being exposed to solvent.

Comparisons of the Interfacial Regions of 2-Cys Prxs. Our present work on AhpC, in conjunction with the structures of TPx-B, TryP, and HBP23, provides a more diverse sampling of the different redox and oligomeric states of
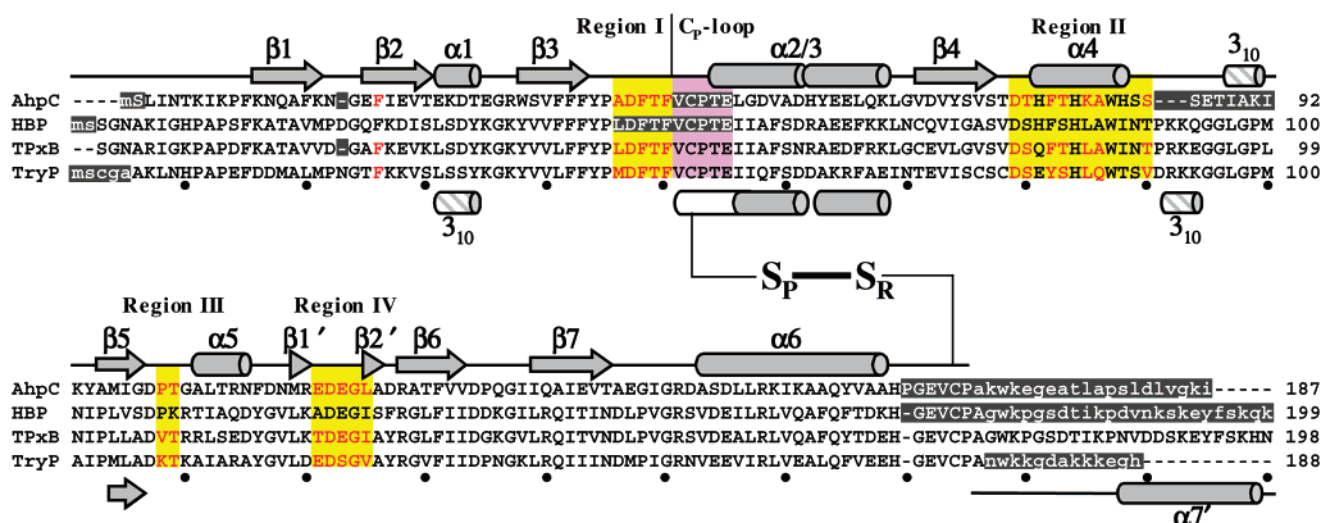
FIGURE 3: Structure-based sequence alignment of 2-Cys Prxs. The top line illustrates the secondary structure elements of AhpC, and the bottom line identifies regions where HBP23, TPx-B, and TryP differ from AhpC. Helices are represented by cylinders [gray for α-helices, white with gray stripes for 3_{10} helices, and solid white denoting the C_P-loop (purple box) that unwinds during oxidation]. β-Strands are represented as gray arrows. Interfacial regions I−IV are boxed in yellow. Residues buried in the oligomerization interface are colored in red, and the redox-active cysteines are identified: S_P (peroxidatic) and S_R (resolving). The disulfide bond shown occurs between subunits of the dimer and not within a single chain. Residues not modeled due to disorder are identified with lower-case letters, and regions not structurally aligned are boxed in dark gray. The helix $\alpha_{2/3}$ is formed from two α-helices abutted against one another (residues 48−55 and 56−62). The equivalent segment was defined as two helices (α_1 and α_2) in TPx-B (*29*) and as a single, bent helix in the other homologues [α_1 in TryP (*34*) and α_2 in HBP23 (*33*)].
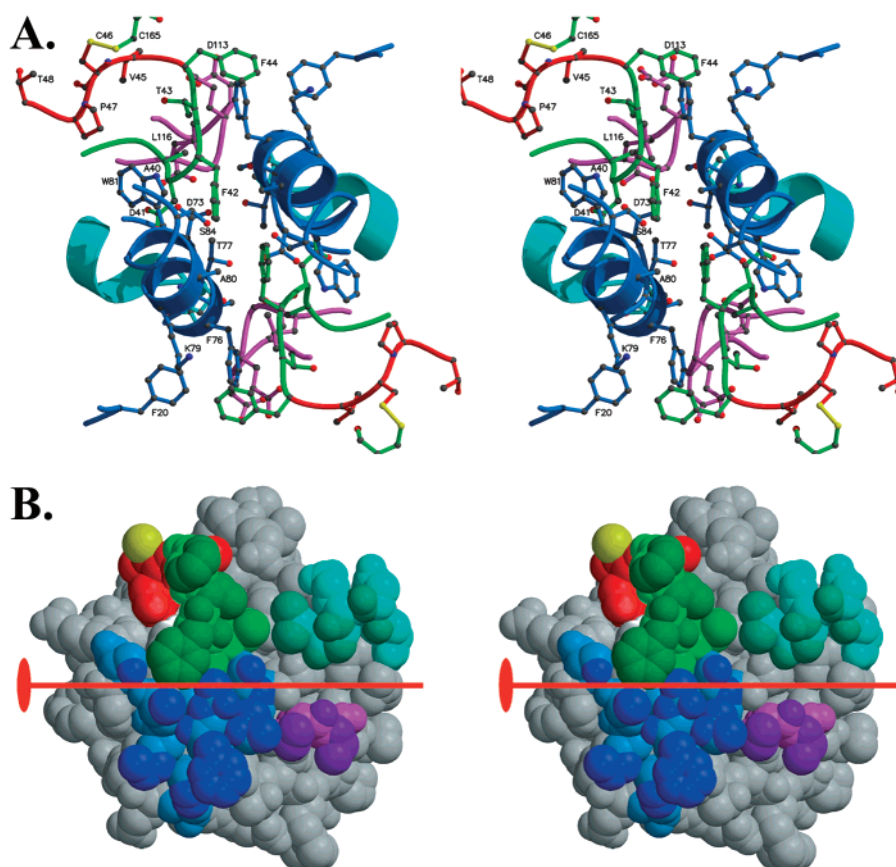

FIGURE 4: Oligomerization interface. (A) Stereo diagram of the oligomerization interface between adjacent α_2 dimers (A−B, A′−B′) in the decamer, with the crystallographic 2-fold axis in the center and normal to the plane of the figure. The C_P-loop (red) is truncated at Thr48. Region I (green), region II (blue), region III (cyan), and region IV (violet) are shown interacting with their complementary regions on the adjacent dimer. (B) CPK space-filling stereo diagram of the cross section of the interface of AhpC. Regions are colored as above, with darker shades representing atoms in contact with the adjacent dimer. The 2-fold symmetry axis is depicted as a red bar. For clarity, the disulfide formed with the resolving cysteine has been omitted. The cavity behind region I (which is occupied by the peroxidatic cysteine in the reduced structure) is highlighted by a soft glow.

2-Cys Prxs than was previously available: TPx-B and TryP represent the reduced, strong $(\alpha_2)_5$ decamer (*29*, *34*), AhpC represents an oxidized, weak $(\alpha_2)_5$ decamer, and HBP23 represents the oxidized, isolated α_2 dimer (*33*). Examining the oligomerization interface between these structures is key to gaining insight into the redox sensitivity of the $(\alpha_2)_5$ oligomeric assembly. The interfaces of TPx-B and TryP have previously been compared and contrasted with HBP23 (*29*, *34*), but our metastable intermediate structure reveals details that could not be resolved by the earlier analyses. Since the TPx-B and TryP structures are very similar, we will use TPx-B in the comparisons, because its structure was determined at a much higher resolution (1.7 vs 3.2 Å for TryP).

Comparisons of TPx-B with AhpC show that the oligomerization interface is essentially the same. The most significant difference between the structures involves the conformation of the five residues immediately following region I and containing the peroxidatic cysteine, hereafter referred to as the C_P-loop (residues 45–49) (Figure 3). In TPx-B, the C_P-loop forms an α-helical turn and packs against the back side of region I (Figure 5A). In this conformation, the peroxidatic active site pocket (*29*) is occupied by the cysteinesulfinic acid, which forms a salt bridge with the conserved Arg119. In AhpC, the C_P-loop is unwound to form a flexible surface loop and expose the peroxidatic cysteine (Cys46), which is disulfide bonded to the resolving cysteine (Cys165′).

Comparisons of AhpC with HBP23 show that the conformations of both the C_P-loop and region I have rearranged, resulting in two new hydrogen bonds (Figure 5B). There are three main components of the conformational change: one, the ψ torsion angle of Asp41 (AhpC numbering) flips +164°, resulting in its carbonyl O pointing into the active site pocket vacated by Cys46; two, rearrangements of residues 42–47 direct the Oγ of Thr43 toward the active site pocket as well; and three, the ϕ torsion angle of Thr48 rotates by 161°, positioning its Oγ for hydrogen bonding with the rotated Asp41-O and Thr43-Oγ. Essentially, the active site pocket vacated by the peroxidatic cysteine has collapsed in HBP23. The result is that region I has pulled away from the interface, disrupting interactions made by Phe42 and Phe44. The movement of Phe42 uncovers Trp82, which in turn adopts a new conformation. These changes result in a restructuring of the interface. A key observation is that our intermediate structure uncouples the rearrangements of the C_P-loop from those that occur in region I and other interface residues.

In addition to the conformational changes, there are also dramatic changes in the mobility of residues at the oligomerization interface (Figure 5C). Remarkably, the mobility patterns of all of the structures are very similar, and the few specific areas that change are readily identified. Comparing the reduced decamer (TPx-B) to the oxidized decamer (AhpC), we observe a large increase in the mobility of both the C_P-loop and region I. The other interfacial regions, II, III, and IV, are essentially unchanged. As expected, in going from the oxidized decamer (AhpC) to the isolated α_2 protomers (HBP23), regions II, III, and IV become less ordered as they are no longer packed in the oligomerization interface. In addition, region I becomes even more disordered. The last two significant differences in main chain mobility are found in the regions after α4 and before α6, which are more ordered in TPx-B than AhpC or HBP23.

This is explained by the structure of TPx-B (*29*), which reveals that those regions are buried by the well-ordered helix α7′ in TPx-B, which is disordered in both the AhpC and HBP23 structures, as well as in the other reduced decamer, TryP.

The C_P-Loop Is the Molecular Switch Controlling Decamer Disassociation and Enzyme Activity. The above comparisons make clear that the conformation and mobility of both the C_P-loop and region I are linked to the oxidation and oligomeric states of the enzymes. The *B*-factor analysis shows that the initial disulfide bond formation involves an increase in the mobility of the C_P-loop and, to a lesser degree, region I. We infer that the higher mobility of region I implies that it is making weaker interactions in the oligomer interface. An explanation for this behavior is found in the local unfolding of the helical C_P-loop, which in TPx-B acts to buttress region I against region II in the interface (Figure 5A). It is possible, we think even likely, that all of the other rearrangements seen in the HBP23 structure occur after dissociation and are not directly responsible for forcing apart the decamer as was suggested previously (*29*, *34*). Instead, the AhpC structure shows that the first structural changes are the local unfolding of the C_P-loop and a coincident increase in mobility for both it and region I and that these occur prior to dissociation.

Interestingly, the converse of the above implies that, for the reduced enzyme, oligomerization favors the folded conformation of the C_P-loop. Because the peroxidatic active site is a cavity lined by residues from the C_P-loop (*29*, *34*), it is possible that the active site will only form properly in the decamer. In this case, one important benefit from decamer formation is the stabilization of the properly folded state of the peroxidatic active site, thereby linking enzyme activity to oligomeric state.

The Oligomerization Model for 2-Cys Peroxiredoxins. Taking these observations together, we propose a structurally detailed catalytic cycle (Figure 6). The cycle begins with the C_P-loop of the reduced enzyme (structure 1) as a redox-sensitive molecular switch in dynamic equilibrium between folded and locally unfolded states (Figure 6, equilibrium 1 ↔ 7). This idea is supported by the structure of TryP (PDB id code 1E2Y), in which three of its subunits have folded C_P-loops (chains C, E, and H), three have unfolded C_P-loops, albeit without the disulfide (chains B, G, and I), and the remaining four (chains A, D, F, and J) are in an intermediate conformation. During peroxidation, the peroxidatic cysteine is oxidized to a reactive sulfenic acid (reaction 1 → 2). What effect a cysteinesulfenic acid has on the local unfolding (equilibrium 2 ↔ 3) is not known. In the locally unfolded conformation, the cysteinesulfenic acid is accessible for attack by the resolving cysteine, and disulfide bond formation traps the C_P-loop in the unfolded conformation (reaction 3 → 4). As more disulfide bonds are formed, the cooperative destabilization of the interface leads to the breakdown of the decamer (equilibrium 4 ↔ 5). As presented, AhpF acts to reduce the free dimers (reaction 5 → 6), which then oligomerize to re-form reduced decamers (equilibrium 6 ↔ 7, 1), completing the catalytic cycle. AhpF may also act to reduce the intact oxidized decamer, but on the basis of an intracellular concentration of AhpC of ca. 5 μM (*72*) and our solution studies, we infer that oxidized AhpC in vivo will exist largely as free dimers.
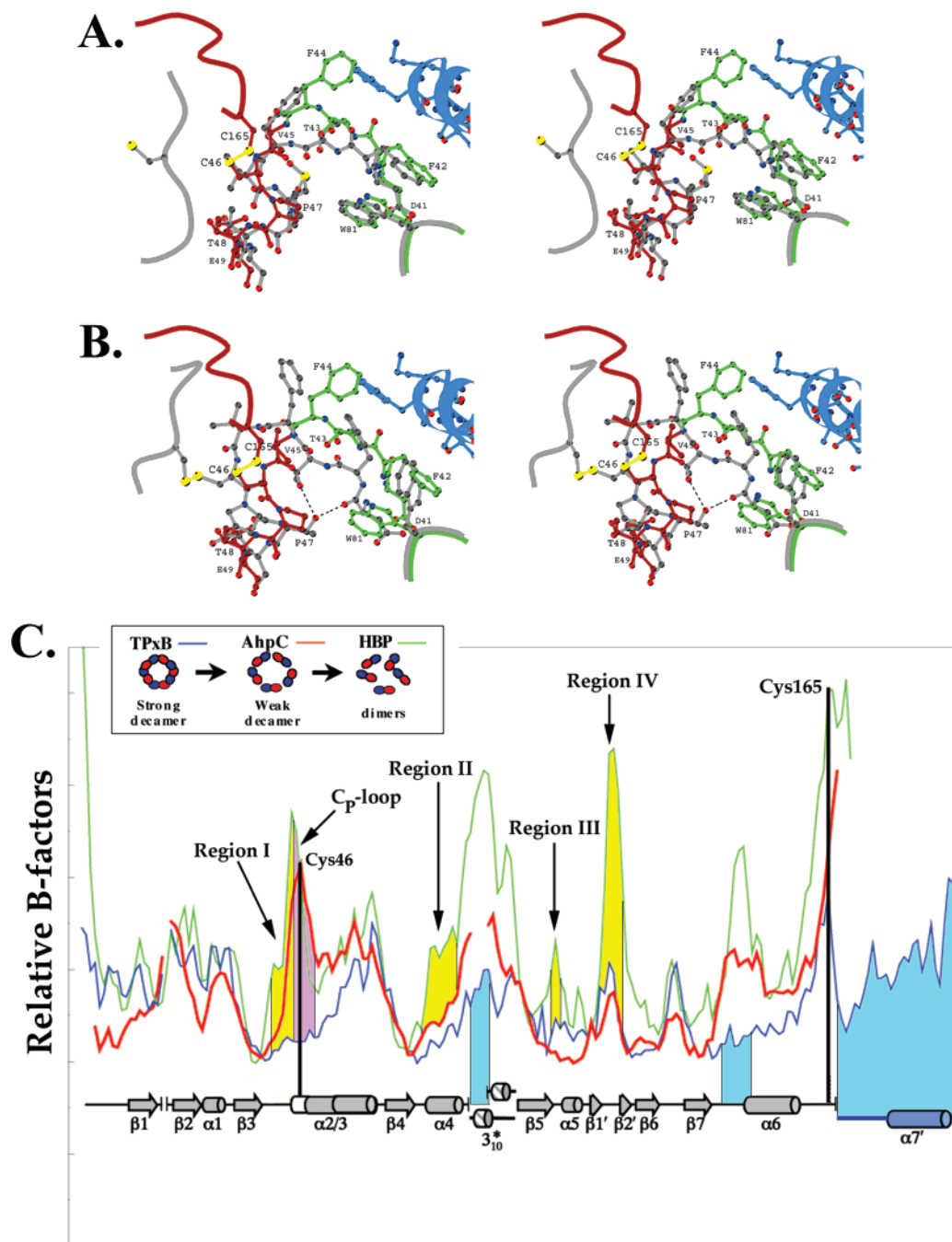
FIGURE 5: Structural differences in the C_P-loops of reduced decameric, oxidized decameric, and oxidized dimeric 2-Cys Prxs. (A) Reduced decamer (TPx-B, gray) versus oxidized decamer (AhpC, red and green). The C_P-loop (red), C-terminus (red), region I (green), and Trp81 (green) of AhpC are overlayed with their counterparts in TPx-B (gray). Also depicted is region II (blue) of the adjacent AhpC dimer to illustrate the oligomerization interface. The unwinding of the C_P-loop in TPx-B has left the peroxidatic active site pocket behind region I vacant (see soft glow in Figure 4B). The interactions between region I and region II are essentially the same. (B) Oxidized decamer (AhpC, as above) versus oxidized dimer (HBP23, gray). The same regions, colors, and orientations as above. The two new hydrogen bonds formed by the rearrangement in HBP23 as region I collapses into the peroxidatic active site pocket are illustrated by dashed lines. (C) Chain mobility of 2-Cys Prxs. Average main chain B-factor plots (for all chains) of AhpC (red), HBP23 (green), and TPx-B (blue) aligned on the basis of structure. Secondary structure elements assigned in Figure 3 are illustrated below the plot, with regions not structurally aligned represented by gaps. The C_P-loop and regions I−IV are identified as well as the peroxidatic and resolving cysteines. Salient differences from which we derive functional insights are shaded as follows; oligomer interface (yellow), C_P-loop (purple), and packing of the C-terminal tail in TPx-B (blue). To simplify comparisons, the B-factors of HBP23 and TPx-B are scaled to AhpC using the ratios 39.74/23.39 or 39.74/21.46, respectively (39.74, 23.39, and 21.46 are the lowest B-factors for AhpC, HBP23, and TPx-B, respectively).

In the case of TPx-B (29), the reactive sulfenic acid is further oxidized to a sulfinic acid, representing a catalytic dead end (reaction 2 → 8). We propose that this overoxidation occurs readily in TPx-B because of the low mobility of the C-terminal tail (see blue regions in Figure 5C). Since structural rearrangements of the C-terminus are required for

disulfide bond formation between C_R and C_PSOH, the lower mobility of the C-terminus would make this step slower in TPx-B and allow peroxide overoxidation of C_PSOH to occur. For TPx-B, evidence suggests that the irreversible overoxidation stabilizes the decamer (29) and that the decamer form associates with membranes (73). The accumulation of
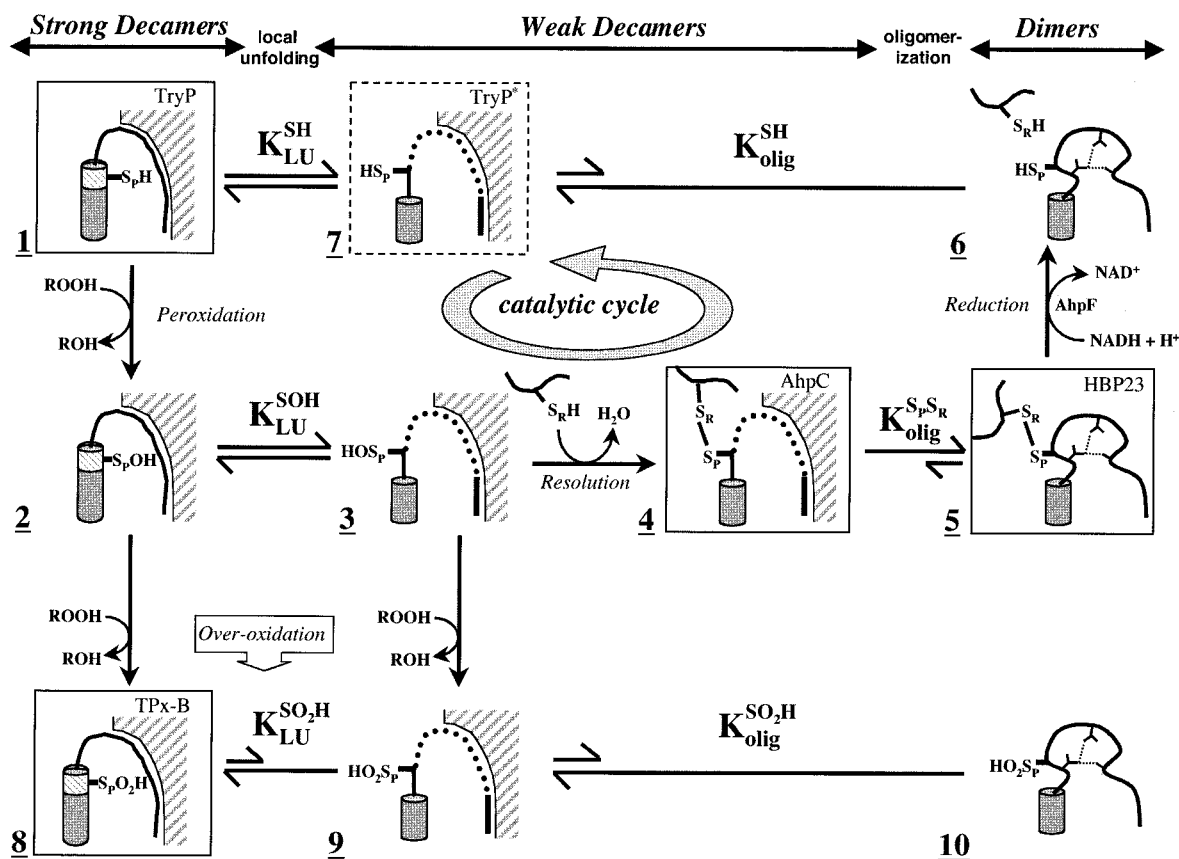
FIGURE 6: Structurally detailed model of the 2-Cys peroxiredoxin catalytic cycle and redox-sensitive oligomerization. Each panel represents a different structure of the proposed mechanism. Boxed structures represent solved crystal structures identified by name in the upper right corner. The dashed box represents an alternate conformation present in the TryP structure. Unboxed structures are proposed intermediates. The C_P-loop containing the peroxidatic cysteine (S_PH), cysteinesulfenic acid (S_POH), or cysteinesulfinic acid (S_PO_2H) is represented in either its helical conformation (hashed cylinder) or extended loop conformation (thick line). Region I is represented as well ordered (curved line), loosely packed (dashed line), or restructured (distorted curved line with hydrogen bonds represented by small dashed lines). Region II of the adjacent dimer is represented by a hashed surface, and panels lacking it indicate dissociation of the decamer. The C-terminus containing the resolving cysteine (S_RH or S_R) is depicted as a thick line. Oxidation steps are represented by one-way arrows, and equilibrium steps are denoted with two-way arrows, with the length relative to the proposed direction of the reaction. The catalytic cycle of AhpC is identified by a circular arrow. See text for further discussion.

inactive, decameric, membrane-associated TPx-B may be physiologically relevant, perhaps acting as a redox sensor to identify oxidatively stressed erythrocytes. Since many 2-Cys peroxiredoxins also serve as redox-sensitive signaling molecules (*22−27, 74*), the dimer to decamer transition may be a general mechanism by which 2-Cys Prxs transduce chemical signals.

A Family of Redox-Sensitive Oligomeric 2-Cys Peroxiredoxins. Our studies have demonstrated that oligomerization of AhpC is redox sensitive, with the reduced enzyme forming the $(\alpha_2)_5$ decamer exclusively and oxidation favoring disassociation to dimers. Our model presents the C_P-loop as the lynchpin in this process, with its removal acting to destabilize the interface between regions I and II. In terms of sequence, region I and the C_P-loop, (x)DFTFVCPTE, and region II, D(T/S)(x)(F/Y)(x)H(xx)W(xx)(S/T/V), are conserved in all 2-Cys Prxs identified to date (prokaryote Prxs and Prxs I−IV in eukaryotes) (for review, see ref *74*), suggesting that $(\alpha_2)_5$ oligomerization is a universal feature of this family.

The full significance of the redox-linked oligomerization of 2-Cys Prxs is not yet understood, but we suggest it has at least two important roles: controlling enzymatic activity and converting a chemical signal into a dramatic structural signal. Our observations extend the work of Choi et al. (*75*), who

recently showed that, for the OxyR transcription factor, activation occurs via peroxide-induced formation of a disulfide bond which triggers a local restructuring and a corresponding shift between tetrameric configurations. Our work provides a second and even more dramatic example of what Choi et al. (*75*) termed protein regulation by "fold editing". On the basis of the detailed catalytic cycle of 2-Cys Prxs (Figure 6), we have begun to design specific mutations that will uncouple the AhpC redox state from oligomerization and serve as tools to probe the role that decamer formation has on function.

NOTE ADDED IN PROOF

Koo et al. (*77*) recently reported that C-terminal mutations of a yeast 2-Cys Prx affect the rate at which it is inactivated by overoxidation. This is consistent with our hypothesis relating the ease of overoxidation of TPx-B to the low mobility of its C-terminal tail.

ACKNOWLEDGMENT

REFERENCES

1. Tartaglia, L. A., Storz, G., Brodsky, M. H., Lai, A., and Ames, B. N. (1990) *J. Biol. Chem. 265*, 10535−10540.

2. Christman, M. F., Morgan, R. W., Jacobson, F. S., and Ames, B. N. (1985) *Cell 41*, 753−762.

3. Morgan, R. W., Christman, M. F., Jacobson, F. S., Storz, G., and Ames, B. N. (1986) *Proc. Natl. Acad. Sci. U.S.A. 83*, 8059−8063.

4. Jacobson, F. S., Morgan, R. W., Christman, M. F., and Ames, B. N. (1989) *J. Biol. Chem. 264*, 1488−1496.

5. Storz, G., Jacobson, F. S., Tartaglia, L. A., Morgan, R. W., Silveira, L. A., and Ames, B. N. (1989) *J. Bacteriol. 171*, 2049−2055.

6. Baker, L. M., Raudonikiene, A., Hoffman, P. S., and Poole, L. B. (2001) *J. Bacteriol. 183*, 1961−1973.

7. Poole, L. B. (1996) *Biochemistry 35*, 65−75.

8. Poole, L. B., and Ellis, H. R. (1996) *Biochemistry 35*, 56−64.

9. Wood, Z. A., Poole, L. B., and Karplus, P. A. (2001) *Biochemistry 40*, 3900−3911.

10. Bieger, B., and Essen, L. O. (2001) *J. Mol. Biol. 307*, 1−8.

11. Li Calzi, M., and Poole, L. B. (1997) *Biochemistry 36*, 13357−13364.

12. Poole, L. B., Godzik, A., Nayeem, A., and Schmitt, J. D. (2000) *Biochemistry 39*, 6602−6615.

13. Poole, L. B., Reynolds, C. M., Wood, Z. A., Karplus, P. A., Ellis, H. R., and Li Calzi, M. (2000) *Eur. J. Biochem. 267*, 6126−6133.

14. Reynolds, C. M., and Poole, L. B. (2000) *Biochemistry 39*, 8859−8869.

15. Reynolds, C. M., and Poole, L. B. (2001) *Biochemistry 40*, 3912−3919.

16. Ellis, H. R., and Poole, L. B. (1997) *Biochemistry 36*, 13349−13356.

17. Ellis, H. R., and Poole, L. B. (1997) *Biochemistry 36*, 15013−15018.

18. Chae, H. Z., and Rhee, S. G. (1994) *Biofactors 4*, 177−180.

19. Rhee, S. G., Kang, S. W., Netto, L. E., Seo, M. S., and Stadtman, E. R. (1999) *Biofactors 10*, 207−209.

20. Chae, H. Z., Kang, S. W., and Rhee, S. G. (1999) *Methods Enzymol. 300*, 219−226.

21. Henkle-Duhrsen, K., and Kampkotter, A. (2001) *Mol. Biochem. Parasitol. 114*, 129−142.

22. Wong, C. M., Chun, A. C., Kok, K. H., Zhou, Y., Fung, P. C., Kung, H. F., Jeang, K. T., and Jin, D. Y. (2000) *Antioxid. Redox Signaling 2*, 507−518.

23. Zhou, Y., Kok, K. H., Chun, A. C., Wong, C. M., Wu, H. W., Lin, M. C., Fung, P. C., Kung, H., and Jin, D. Y. (2000) *Biochem. Biophys. Res. Commun. 268*, 921−927.

24. Kang, S. W., Chae, H. Z., Seo, M. S., Kim, K., Baines, I. C., and Rhee, S. G. (1998) *J. Biol. Chem. 273*, 6297−6302.

25. Sullivan, D. M., Wehr, N. B., Fergusson, M. M., Levine, R. L., and Finkel, T. (2000) *Biochemistry 39*, 11121−11128.

26. Seo, M. S., Kang, S. W., Kim, K., Baines, I. C., Lee, T. H., and Rhee, S. G. (2000) *J. Biol. Chem. 275*, 20346−20354.

27. Chung, Y. M., Yoo, Y. D., Park, J. K., Kim, Y. T., and Kim, H. J. (2001) *Anticancer Res. 21*, 1129−1133.

28. Park, S. H., Chung, Y. M., Lee, Y. S., Kim, H. J., Kim, J. S., Chae, H. Z., and Yoo, Y. D. (2000) *Clin. Cancer Res. 6*, 4915−4920.

29. Schroder, E., Littlechild, J. A., Lebedev, A. A., Errington, N., Vagin, A. A., and Isupov, M. N. (2000) *Struct. Folding Des. 8*, 605−615.

30. Kitano, K., Niimura, Y., Nishiyama, Y., and Miki, K. (1999) *J. Biochem. (Tokyo) 126*, 313−319.

31. Kristensen, P., Rasmussen, D. E., and Kristensen, B. I. (1999) *Biochem. Biophys. Res. Commun. 262*, 127−131.

32. Chauhan, R., and Mande, S. C. (2001) *Biochem. J. 354*, 209−215.

33. Hirotsu, S., Abe, Y., Okada, K., Nagahara, N., Hori, H., Nishino, T., and Hakoshima, T. (1999) *Proc. Natl. Acad. Sci. U.S.A. 96*, 12333−12338.

34. Alphey, M. S., Bond, C. S., Tetaud, E., Fairlamb, A. H., and Hunter, W. N. (2000) *J. Mol. Biol. 300*, 903−916.

35. Schroder, E., Willis, A. C., and Ponting, C. P. (1998) *Biochim. Biophys. Acta 1383*, 279−291.

36. Ramakrishnan, V., Finch, J. T., Graziano, V., Lee, P. L., and Sweet, R. M. (1993) *Nature 362*, 219−223.

37. Laue, T. M., Shah, B. D., Ridgeway, T. M., and Pelletier, S. L. (1992) in *Analytical ultracentrifugation in biochemistry and polymer science* (Harding, S. E., Rowe, A. J., and Horton, J. C., Eds.) pp 90−125, The Royal Society of Chemistry, Cambridge.

38. Philo, J. S. (2000) *Anal. Biochem. 279*, 151−163.

39. Philo, J. S. (1997) *Biophys. J. 72*, 435−444.

40. Stafford, W. F., III (1992) *Anal. Biochem. 203*, 295−301.

41. Van Holde, K. E. (1971) in *Physical Biochemistry*, pp 110−136, Prentice-Hall, Englewood Cliffs, NJ.

42. Johnson, M. L., Correia, J. J., Yphantis, D. A., and Halvorson, H. R. (1981) *Biophys. J. 36*, 575−588.

43. Hantgan, R. R., Paumi, C., Rocco, M., and Weisel, J. W. (1999) *Biochemistry 38*, 14461−14474.

44. Johnson, C. S., and Gabriel, D. A. (1981) in *Spectroscopy in Biochemistry* (Bell, J. E., Ed.) pp 177−272, CRC Press, Boca Raton, FL.

45. Spotorno, B., Piccinini, L., Tassara, G., Ruggiero, C., Nardini, M., Molina, F., and Rocco, M. (1997) *Eur. Biophys. J. 25*, 373−384.

46. Hantgan, R. R., Braaten, J. V., and Rocco, M. (1993) *Biochemistry 32*, 3935−3941.

47. Jancarik, J., and Kim, S. H. (1991) *J. Appl. Crystallogr. 24*, 409−411.

48. Rodgers, D. W. (1997) *Methods Enzymol. 276*, 183−203.

49. Otwinowski, Z., and Minor, W. (1996) *Methods Enzymol. 276*, 307−326.

50. Diederichs, K., and Karplus, P. A. (1997) *Nat. Struct. Biol. 4*, 269−275.

51. Collaborative Computational Project (1994) *Acta Crystallogr., Sect. D 50*, 760−763.

52. Kissel, L. P., R. H. (1990) *Acta Crystallogr. A46*, 170−175.

53. Cromer, D. T. (1983) *J. Appl. Crystallogr. 16*, 437.

54. Terwilliger, T. C., and Berendzen, J. (1999) *Acta Crystallogr., Sect. D 55*, 849−861.

55. Furey, W., and Swaminathan, S. (1997) *Methods Enzymol. 277B*, 590−620.

56. Brunger, A. T. (1992) *X-PLOR (Version 3.8)*, Yale University, New Haven, CT.

57. Sack, J. S., and Quiocho, F. A. (1997) *Methods Enzymol. 277*, 158−173.

58. Jones, T. A., Zou, J. Y. Cowan, S. W., and Kjeldgaard, M. (1991) *Acta Crystallogr. 47*, 110−119.

59. Kleywegt, G. J., and Read, R. J. (1997) *Structure 5*, 1557−1569.

60. Jones, T. A. (1992) *A yaap, asap, @#*? A set of averaging programs*, SERC Daresbury Laboratory, Warrington.

61. Kleywegt, G. J., and Jones, T. A. (1994) in *From First Map to Final Model* (Bailey, S., Hubbard, R., and Walter, D., Eds.) pp 59−66, SERC Daresbury Laboratory, Warrington, England.

62. Brunger, A. T., Adams, P. D., Clore, G. M., DeLano, W. L., Gros, P., Grosse-Kunstleve, R. W., Jiang, J. S., Kuszewski, J., Nilges, M., Pannu, N. S., Read, R. J., Rice, L. M., Simonson, T., and Warren, G. L. (1998) *Acta Crystallogr., Sect. D 54*, 905−921.

63. Brunger, A. T. (1997) *Methods Enzymol. 277B*, 366−396.

64. Laskowski, R. A., Macarthur, M. W., Moss, D. S., and Thornton, J. M. (1993) *J. Appl. Crystallogr. 26*, 283−291.

65. Kabsch, W., and Sander, C. (1983) *Biopolymers 22*, 2577−2637.

66. Westhead, D. R., Slidel, T. W., Flores, T. P., and Thornton, J. M. (1999) *Protein Sci. 8*, 897−904.

67. Smith, R. F., and Smith, T. F. (1990) *Proc. Natl. Acad. Sci. U.S.A. 87*, 118−122.

68. Smith, R. F., and Smith, T. F. (1992) *Protein Eng. 5*, 35−41.

69. Kraulis, P. (1991) *J. Appl. Crystallogr. 24*, 946−950.

70. Esnouf, R. M. (1997) *J. Mol. Graphics 15*, 132−134.

71. Merrit, E. A., and Bacon, D. J. (1997) *Methods Enzymol. 277*, 505−524.

72. Link, A. J., Robison, K., and Church, G. M. (1997) *Electrophoresis 18*, 1259−1313.

73. Cha, M. K., Yun, C. H., and Kim, I. H. (2000) *Biochemistry 39*, 6944−6950.

74. Butterfield, L. H., Merino, A., Golub, S. H., and Shau, H. (1999) *Antioxid. Redox Signaling 1*, 385−402.

75. Choi, H., Kim, S., Mukhopadhyay, P., Cho, S., Woo, J., Storz, G., and Ryu, S. (2001) *Cell 105*, 103−113.

76. Hendrickson, W. A. (1991) *Science 254*, 51−58.

77. Koo, K. H., Lee, S., Jeong, S. Y., Kim, E. T., Kim, H. J., Kim, K., Song, K., and Chae, H. Z. (2002) *Arch. Biochem. Biophys. 397*, 312−318.